PERIDYNAMICS ANALYSIS OF THE
NANOSCALE FRICTION AND WEAR PROPERTIES
OF AMORPHOUS CARBON THIN FILMS

Sayna Ebrahimi, David J. Steigmann and Kyriakos Komvopoulos

msp

PERIDYNAMICS ANALYSIS OF THE
NANOSCALE FRICTION AND WEAR PROPERTIES
OF AMORPHOUS CARBON THIN FILMS

SAYNA EBRAHIMI, DAVID J. STEIGMANN AND KYRIAKOS KOMVOPOULOS

State-based peridynamics theory was used to study the nanoscale friction and wear behavior of thin films of amorphous carbon used as protective overcoats in hard-disk drives. Numerical results of the coefficient of friction and wear depth are shown to be in good agreement with published experimental results. Although long-range forces are not considered in the analysis, the results indicate that the present approach yields fairly accurate estimates of the coefficient of friction and wear depth for films of thickness larger than 10 nm and a grid size of 1.6 nm. The results of this study demonstrate that peridynamics theory can be used to analyze various nanoscale friction and wear phenomena without being limited by the excessive computational time and convergence difficulties encountered with traditional numerical techniques, such as the finite element method.

1. Introduction

Thin films are used as protective overcoats in a wide range of applications where the tribological properties of proximal surfaces are of paramount importance to the functionality and endurance of mechanical components possessing contact interfaces. For example, thin films of amorphous carbon (a-C) play a critical role in the reliability and performance of magnetic recording devices because they protect the magnetic head and hard disk surfaces against mechanical wear during intermittent contact and inhibit corrosion of the magnetic medium of the hard disk. Because of the extremely small a-C film thickness and the occurrence of head-disk surface interactions at nanoscopic surface protrusions (asperities), knowledge of the nanoscale tribological and mechanical properties of thin a-C films is of high technological importance.

The nanomechanical/tribological properties of a-C films are greatly affected by the type of carbon atom hybridization and the hydrogen content. Other elements (e.g., Si, N, B, F, and O) can be added to modify the electromechanical properties of a-C films [Charitidis 2010]. The structure and elemental content of a-C films strongly depend on the intricacies of the deposition process, which controls film nucleation and growth [Lifshitz 1996; Grill 1999; Charitidis 2010]. Thus, small variations in the deposition conditions may result in vastly different film properties. In view of the time-consuming experimental techniques available for nanoscale mechanical and tribological testing of thin films, alternative approaches must be used to examine the effects of structural changes on the resulting film properties.

High contents of tetrahedral carbon atom hybridization (sp^3) characterize the structure of a-C films exhibiting diamond-like behavior, whereas high contents of trigonal carbon atom hybridization (sp^2)

generally produce graphite-like film behavior. A continuum description does not account for local differences in nanostructure [Luan and Robbins 2005], whereas molecular dynamics (MD) is limited by high computational cost, model size, and type of potential function used to describe atomic interaction [Alder and Wainwright 1959]. Therefore, nonlocal computational approaches, which are not subjected to the aforementioned restrictions, must be developed to enhance the study of the interdependence of structure and material behavior at the nanoscale.

Peridynamics [Silling 2000] is a relatively new theory which promises to bridge the material gap in computational mechanics. Peridynamics is a continuum version of MD which uses integral equations of motion to offset complexities associated with material discontinuities (e.g., defects, edges, and sharp corners) instead of the conventional partial differential equations used in classical mechanics and does not rely on *a priori* assumed defect or damage criteria (e.g., crack growth direction). Because of the mathematical simplicity and computational affordability, peridynamics has been used to analyze various computationally intense problems, such as dynamic fracture in brittle [Ha and Bobaru 2010; 2011; Bobaru and Hu 2012; Liu and Hong 2012; Lipton 2014] and composite [Askari et al. 2006; Xu et al. 2008; Kilic et al. 2009; Hu et al. 2011; 2012] materials, multiscale damage [Askari et al. 2008; Alali and Lipton 2012], and damage of nanofiber networks, including long-range effects of van der Waals forces on nanofiber deformation [Bobaru and Silling 2004; Silling and Bobaru 2005; Bobaru 2007; Bobaru et al. 2011]. Moreover, peridynamics has been used in failure analyses dealing with thin film cracking in electronic packaging [Agwai et al. 2008; 2009; 2011] and also in conjunction with atomic force microscopy and nanoindentation techniques to determine the mechanical properties of ultrathin films [Celik et al. 2009].

The objective of this study is to introduce a two-dimensional (2D) peridynamics analysis of the nanotribological behavior of thin *a*-C films. Simulation results of the coefficient of friction and depth of wear track due to a rigid (diamond) tip sliding against *a*-C films of different thickness and nanomechanical properties are presented and compared with experimental results of a previous study [Lu and Komvopoulos 2001] to validate the accuracy of the developed peridynamics models.

2. State-based peridynamics formulation

Peridynamics is a theory of mechanics which uses a finite number of particles to discretize a deformable solid body. Particle interaction is modeled within a predefined distance, referred to as the horizon. Because the governing equations in peridynamics are integrals of particle motion, material discontinuities and high strain gradients do not present computational obstacles. The main peridynamics approaches can be classified in bond-based and state-based formulations. Bond-based peridynamics presumes the existence of a pairwise force function between any two particles, which is independent of the deformation associated with other particles [Silling 2000] and has been developed for a Poisson's ratio of 0.33 and 0.25 for 2D and three-dimensional (3D) problems, respectively. State-based peridynamics relies on a more general theory, which uses a more comprehensive constitutive model derived based on force- and deformation-state concepts [Silling et al. 2007]. To obtain the force state at each particle, the deformation (stretching) of all bonds within the horizon of each particle are considered without assuming a specific value of the Poisson's ratio. Similarities between state-based peridynamics and continuum theory have been reported [Silling et al. 2007; Lehoucq and Silling 2008], including the convergence of state-based peridynamics to classical elasticity theory [Silling and Lehoucq 2008].

The general 3D peridynamics equation of motion is given by [Silling et al. 2007]

$$\rho(\boldsymbol{x}_i)\ddot{\boldsymbol{u}}(\boldsymbol{x}_i, t) = \int_{\mathscr{H}} \left(\underline{\boldsymbol{T}}[\boldsymbol{x}_i, t]\langle \boldsymbol{x}_j - \boldsymbol{x}_i \rangle - \underline{\boldsymbol{T}}[\boldsymbol{x}_j, t]\langle \boldsymbol{x}_i - \boldsymbol{x}_j \rangle \right) \mathrm{d}V_j + \boldsymbol{b}(\boldsymbol{x}_i, t), \tag{1}$$

where ρ is the mass density, $\boldsymbol{x}_i$ and $\boldsymbol{x}_j$ are the position vectors of particles i and j, respectively, $\boldsymbol{u}$ is the displacement field, $\mathscr{H}$ is the domain of the spherical horizon with a radius δ, $\underline{\boldsymbol{T}}$ is the force vector state field, $\boldsymbol{b}$ is the body force density field, t is the time, and $\mathrm{d}V_j$ is the volume of particle j. In the present analysis, the deformable materials are assumed to be ordinary, implying that the force between two particles acts in the bond direction.

For ordinary materials, the force vector is given by [Silling et al. 2007]

$$\underline{\boldsymbol{T}} = \underline{t}\underline{\boldsymbol{M}}, \tag{2}$$

where $\underline{t}$ is the scalar force state and $\underline{\boldsymbol{M}}$ is the deformation direction vector. In the linear peridynamics solid (LPS) model, the force scalar state is defined by [Silling et al. 2007]

$$\underline{t} = \frac{3K\theta[\boldsymbol{x}, t]}{m[\boldsymbol{x}]}\underline{\omega}\langle \boldsymbol{\xi} \rangle \underline{x}\langle \boldsymbol{\xi} \rangle + \frac{15G}{m[\boldsymbol{x}]}\underline{\omega}\langle \boldsymbol{\xi} \rangle \underline{e}^d[\boldsymbol{x}, t], \tag{3}$$

where K and G are the bulk and shear modulus, respectively, θ is the dilatation, m is the weighted volume, $\underline{e}^d$ is the deviatoric component of the extension scalar state $\underline{e}$, and $\underline{\omega}$ is the influence function. These parameters can be defined, following [Silling et al. 2007], as:

$$\theta[\boldsymbol{x}, t] = \frac{3}{m[\boldsymbol{x}]} \int_{\mathscr{H}} \underline{\omega}\langle \boldsymbol{\xi} \rangle \underline{x}\langle \boldsymbol{\xi} \rangle \underline{e}[\boldsymbol{x}, t]\langle \boldsymbol{\xi} \rangle \, \mathrm{d}V, \tag{4}$$

$$m[\boldsymbol{x}] = \int_{\mathscr{H}} \underline{\omega}\langle \boldsymbol{\xi} \rangle \underline{x}\langle \boldsymbol{\xi} \rangle \underline{x}\langle \boldsymbol{\xi} \rangle \, \mathrm{d}V, \tag{5}$$

$$\underline{e}[\boldsymbol{x}, t]\langle \boldsymbol{\xi} \rangle = \|\boldsymbol{\xi} + \boldsymbol{\eta}\| - \|\boldsymbol{\xi}\|, \tag{6}$$

$$\underline{e}^d[\boldsymbol{x}, t]\langle \boldsymbol{\xi} \rangle = \underline{e}[\boldsymbol{x}, t]\langle \boldsymbol{\xi} \rangle - \underline{e}^i[\boldsymbol{x}, t]\langle \boldsymbol{\xi} \rangle = \underline{e}[\boldsymbol{x}, t]\langle \boldsymbol{\xi} \rangle - \tfrac{1}{3}\theta[\boldsymbol{x}, t]\underline{x}\langle \boldsymbol{\xi} \rangle, \tag{7}$$

where $\boldsymbol{\xi} = \boldsymbol{x}_j - \boldsymbol{x}_i$ is the relative position vector between particles i and j in the reference configuration and $\boldsymbol{\eta} = \boldsymbol{u}(\boldsymbol{x}_j, t) - \boldsymbol{u}(\boldsymbol{x}_i, t)$ is the relative displacement vector between particles i and j at time t.

Because of the highly disordered structure of a-C films [Charitidis 2010], they can be modeled as isotropic materials with an influence function $\underline{\omega}\langle \boldsymbol{\xi} \rangle = 1/\|\boldsymbol{\xi}\|$, as suggested elsewhere [Parks et al. 2010].

Damage is assumed to occur when bond stretching exceeds a predefined critical stretch s_c, given by [Silling and Askari 2005; Ha and Bobaru 2011]

$$s_c = \sqrt{4\pi G_I / 9E\delta}, \tag{8}$$

where G_I is the critical energy release rate corresponding to the mode I stress intensity factor K_I (i.e., $G_I = K_I^2/E'$, where $E' = E$ (plane stress) or $E/(1 - v^2)$ (plane strain)). Equation (8) indicates that s_c is a function of the material properties and the characteristic length scale of the analyzed body, i.e., the horizon radius δ.

Damage at a given material point (particle) is defined as the ratio of the number of broken bonds to the total number of bonds D. Because D assumes values between 0 (no damage) and 1 (full damage)

[Silling and Askari 2005], it can be used as a damage index to characterize the extent of material removal ($D = 1$) and the evolution of permanent damage ($0 < D < 1$) in the wear model.

3. Body discretization and computational details

To obtain a solution for the 2D version of (1), the body is discretized by a uniform grid ($\Delta x = \Delta y$) and the integral is replaced by a summation including all interacting particles within the horizon of a given particle. Thus, (1) can be expressed as

$$\rho_i \ddot{\boldsymbol{u}}_i^n = \sum_{j=1}^{N_{\mathscr{H}}} \mathscr{F}(\boldsymbol{x}_i^n, \boldsymbol{x}_j^n, \boldsymbol{x}_i^{n-1}, \boldsymbol{x}_j^{n-1}) V_j + \boldsymbol{b}_i^n, \qquad (9)$$

where the superscripts denote the time step and $N_{\mathscr{H}}$ is the total number of particles interacting with the particle of interest within its horizon. Time integration of (9) using the central difference method yields the position and velocity of each particle at time step ($n + 1$). The nodal area of the particles lying on the horizon boundaries is accordingly modified [Parks et al. 2008].

In addition to the force vector state obtained from (2), short-range forces are also included in the present analysis by introducing a short-range particle interaction distance

$$d_{pi} = \min\{0.9\|\boldsymbol{x}_p - \boldsymbol{x}_i\|, 1.35(r_p + r_i)\},$$

where $\boldsymbol{x}_p$ and r_p are the position and radius of particle p in the vicinity of particle i, respectively, and r_i is the radius of particle i, which is set equal to one-half of the grid size (i.e., $r_i = \frac{1}{2}\Delta x$) [Parks et al. 2010]. Long-range forces may also have a strong effect on nanoscale deformation and, despite the continuum nature of peridynamics, it is possible to incorporate potential force functions from MD analysis in the force state of peridynamics [Silling and Bobaru 2005; Bobaru 2007; Bobaru et al. 2011]. However, for a separation distance of 2 nm, long-range forces reach ~10% of their peak values [Bobaru 2007]. Consequently, because the grid size used in the present analysis is less than 2 nm (see Section 4 for details), long-range forces are not considered for simplicity.

4. Peridynamics friction and wear models

State-based peridynamics friction and wear models are presented in this section and simulation results are compared with published experimental results of the nanoscale tribological properties of thin a-C films [Lu and Komvopoulos 2001] to illustrate the validity of the developed models. A 2D analysis of the sliding process is valid provided the depth of penetration is significantly less than the width of the resulting plowing (wear) track [Komvopoulos et al. 1985]. Since in all simulation cases the ratio of the wear depth to the wear track width is less than 0.1, a 2D peridynamics analysis of the sliding friction and wear processes is justifiable. All simulations were performed with a custom-made peridynamics code written in Fortran 90/95 and executed on a Linux platform with a quad-core 2.33 GHz Intel Xeon E5345 CPU.

4.1. *Friction model.* Figure 1 schematically shows a rigid spherical tip of radius R under normal load P, which is sliding against a thin a-C film firmly attached to a thick Si substrate. Because of the high elastic modulus of diamond, in all numerical simulations the tip is modeled as rigid. The center of the tip is initially set at a distance equal to $R - \frac{1}{2}\Delta x$ from the film surface. Short-range forces inhibit the
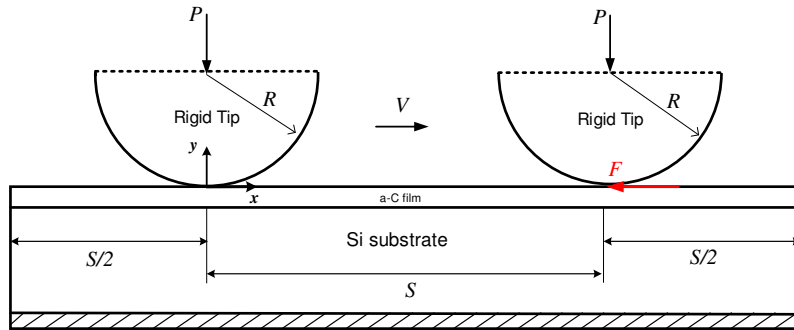
Figure 1. Schematic of peridynamics friction model of a spherical diamond (rigid) tip sliding at a constant velocity V against a thin a-C film, which is firmly adhered to a thick Si substrate. The tip slides from left ($x/S = 0$) to right ($x/S = 1$) through a total distance S. The shaded layer at the bottom of the substrate is modeled as rigid. The coefficient of friction is obtained as the ratio of the computed tangential (friction) force F, which opposes tip sliding, and the applied normal load P. The film thickness and the tip radius are not drawn to scale.

development of particle-particle distances less than d_{pi}, defined in Section 3. Both film and substrate materials are assumed to be isotropic, predominantly exhibiting brittle behavior. The elastic properties, density, and critical stretch of the Si substrate are given in Table 1, whereas the thickness, root-mean-square (rms) roughness, elastic properties, and density of all a-C films examined in this study are given

Material	Elastic modulus[a] (GPa)	Poisson's ratio[a]	Density[a] (g/cm³)	Critical stretch[b]
Silicon	132	0.278	2.329	0.01

Table 1. Mechanical properties and critical stretch of Si substrate. [a]Ref. [Lu and Komvopoulos 2001]. [b]Ref. [Agwai et al. 2011].

Film #	Thickness[a] (nm)	Roughness,[a] rms (nm)	Elastic modulus[a] (GPa)	Poisson's ratio[a]	Density (g/cm³)	# particles (film)	# particles (substrate)
1	31	0.51	105	0.278	3.139	5000 × 19	5000 × 606
2	34	0.20	197	0.278	4.058	5000 × 21	5000 × 604
3	39	0.15	206	0.278	4.143	5000 × 24	5000 × 601
4	53	0.27	139	0.278	3.500	5000 × 33	5000 × 592
5	59	0.23	101	0.278	3.094	5000 × 36	5000 × 589
6	69	0.15	192	0.278	4.017	5000 × 43	5000 × 582
7	95	0.24	155	0.278	3.661	5000 × 59	5000 × 566

Table 2. Thickness, roughness, elastic properties, and density of a-C films and number of film and substrate particles used in the peridynamics friction analysis. [a]Ref. [Lu and Komvopoulos 2001].

in Table 2. The film density was calculated from the relation $\rho = 1.37 + E^{2/3}/44.65$, where ρ and E are given in g/cm^3 and GPa, respectively [Casiraghi et al. 2007]. The number of particles used to discretize the film and substrate media in each friction simulation are also given in Table 2. In all friction simulations, the tip radius is equal to $20 \, \mu$m.

To enhance the convergence, load-control sliding experiments were simulated by the following method. First, the normal load was incrementally applied using several time steps until the desired load (in the range of 50–400 μN) was reached. This incremental loading procedure is similar (though faster) to that used in the experimental study [Lu and Komvopoulos 2001]. Subsequently, the tip was traversed in the x-direction at a constant velocity $V = 0.4 \, \mu$m/s through a total distance $S = 4 \, \mu$m. To avoid boundary effects on the friction results, the distance of the left and right boundaries of the discretized domain from the initial ($x/S = 0$) and final ($x/S = 1$) tip positions was set equal to $S/2$ (Figure 1). An adaptive dynamic relaxation (ADR) method similar to that presented in [Kilic and Madenci 2010], which was accordingly modified for state-based formulation, was used in the friction analysis. The time step in the ADR analysis of friction was set equal to 0.01 s. Artificial damping was used in the equations of particle and tip motion. For the calculation of the damping coefficient of the rigid tip, the stiffness was increased by a factor of 10 to account for the rigidity of the tip. Similar to the friction experiments reported in [Lu and Komvopoulos 2001], only elastic deformation is modeled in the friction simulations, i.e., irreversible damage such as bond breakage is not included in the friction model. The initial boundary conditions used for time integration are zero displacements and velocities in all directions at all particles and the tip center. Films of thickness larger than 10 nm are examined because the grid size is less than 2 nm. In addition, because the rms roughness of the films (in the range of 0.15–0.51 nm [Lu and Komvopoulos 2001]) is significantly smaller than the grid size, both film and substrate media are modeled as perfectly smooth.

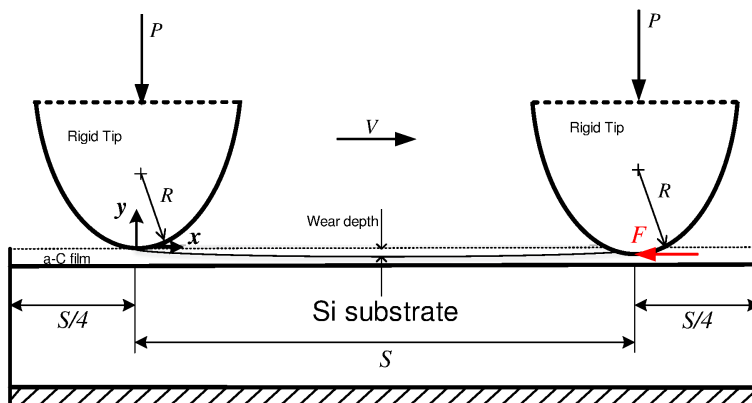**Figure 2.** Schematic of peridynamics wear model of a sharp conospherical diamond (rigid) tip under a normal load P sliding at a constant velocity V and plowing through a thin a-C film, which is firmly attached to a thick Si substrate. The tip slides against the film surface from left ($x/S = 0$) to right ($x/S = 1$) through a total distance S. The shaded layer at the bottom of the substrate is modeled as rigid. The film thickness and the tip radius are not drawn to scale.

Film #	Thickness[a] (nm)	Roughness,[a] rms (nm)	Elastic modulus[a] (GPa)	Poisson's ratio[a]	Density (g/cm^3)	Critical stretch	# particles (film)	# particles (substrate)
8	17	0.19	113	0.278	3.230	0.0125	937×10	937×615
9	22	0.18	203	0.278	4.115	0.0125	937×13	937×612
10	10	0.20	226	0.278	4.317	0.0125	937×6	937×619

Table 3. Thickness, roughness, elastic properties, density, and critical stretch of a-C films and number of film and substrate particles used in the peridynamics wear analysis. [a]Ref. [Lu and Komvopoulos 2001].

4.2. *Wear model.* Figure 2 shows a schematic of the wear model consisting of a sharp rigid (diamond) conospherical probe with a tip radius R plowing through an a-C film, which is firmly attached to a thick Si substrate. After incremental loading of the probe to the desired normal load $P = 10\,\mu\text{N}$ (load-control simulations) at $x/S = 0$, the probe was traversed in the x-direction at a constant velocity $V = 4\,\mu\text{m/s}$ through a total distance $S = 1\,\mu\text{m}$ and was finally unloaded at $x/S = 1$. To avoid boundary effects on the wear results, the distance of the left and right boundaries of the discretized domain from the initial ($x/S = 0$) and final ($x/S = 1$) tip positions was set equal to $S/4$. The thickness, rms roughness, elastic properties, density, and critical stretch of the a-C films analyzed with the wear model and the number of particles used to discretize the film and the substrate are given in Table 3. In all wear simulations, the probe tip radius is equal to $1\,\mu\text{m}$ and the initial displacements and velocities of the tip and all particles are set equal to zero. The previously mentioned ADR technique [Kilic and Madenci 2010] with a time step of 0.001 s was also used in the wear analysis.

In the wear simulations, irreversible damage in the wake of the plowing tip comprises bond breakage. Therefore, a critical bond stretch was used to capture bond breakage. In addition to the critical bond stretch of the substrate (Table 1) and film (Table 3) materials, a conservative estimate of the critical bond stretch of the a-C/Si interface was obtained from (8), where E is the elastic modulus of the substrate and G_I is the strain energy release rate due to indentation of the film by a conospherical diamond indenter, which is equal to $0.037\,\text{J/m}^2$ [Marshall and Evans 1984; Volinsky et al. 2002]. Using (8), the critical stretch of the a-C/diamond interface was found to be equal to 0.007. The depth of the wear track on the film surface was determined by calculating the average displacement of irreversibly deformed ($0 < D < 1$) particle layers of the film medium along the plowing path after the unloading of the probe tip.

5. Results and discussion

Simulation results obtained with the peridynamics friction and wear models are presented in this section in conjunction with experimental results from a previous experimental study [Lu and Komvopoulos 2001] to validate both peridynamics models.

5.1. *Coefficient of friction.* The coefficient of friction is defined as the ratio of the tangential (friction) force and the applied normal load. At each time step, the friction force was calculated as the tangential component of the total force generated by the sliding action of the tip; thus, a coefficient of friction was computed at each time step. An overall coefficient of friction was calculated for each a-C film as the average of all friction coefficient data.

δ (nm)	m	Coefficient of friction
8	3.5	0.1421
8	4.0	0.1526
8	4.5	0.1567
8	5.0	0.1591
8	5.5	0.1456

Table 4. Coefficient of friction results from m-convergence tests.

Similar to local numerical methods, determining an appropriate grid size in peridynamics requires convergence testing [Bobaru et al. 2009; Bobaru and Hu 2012]. Among various convergence tests, the m-convergence test was used in the peridynamics friction model to calculate the coefficient of friction. The δ-convergence test was not used because the decrease of the horizon radius to zero (i.e., no length scale) should yield solutions converging to classical elasticity solutions, which not only do not hold at the nanoscale [Luan and Robbins 2005] but are also length-scale independent. In the m-convergence test, δ is fixed whereas $m = \delta/\Delta x$ is gradually increased until the solution converges to an exact nonlocal peridynamics solution obtained for fixed δ [Bobaru et al. 2009]. Table 4 shows results from m-convergence tests for film #7 (Table 2), $P = 400\ \mu N$, $\delta = 8$ nm, and m in the range of 3.5-5.5. The coefficient of friction diverges with the increase of m from 5.0 to 5.5, suggesting an increasing effect of long-range forces. Therefore, $m = 5.0$ (i.e., $\Delta x = 1.6$ nm) was used in the present peridynamics analysis. Because the focus of this study is the analysis of thin a-C films, the convergence test was only carried out for the a-C film.

Table 5 shows a comparison between peridynamics and experimental results of the coefficient of friction of a-C films with different thickness and rms roughness for P in the range of 50–400 μN. Even though the films were modeled to have ideally smooth surfaces, the agreement between numerical and experimental results is very good. It is noted that the experimental coefficients of friction represent averages of 300 data acquired along the entire sliding track and that the scatter in the measurements increases with the decrease of the normal load, yielding standard deviation values in the range of 0.05–0.08 [Lu and Komvopoulos 2001].
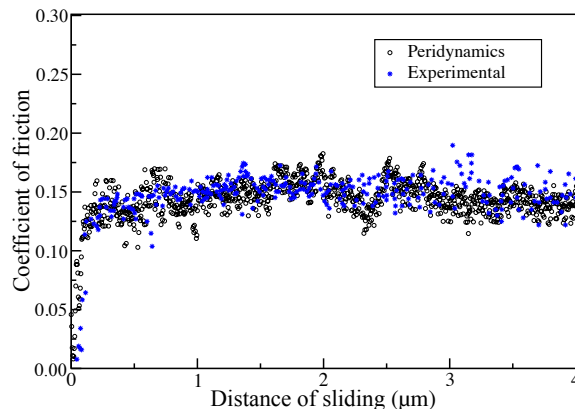

Figure 3. Peridynamics and experimental results [Lu and Komvopoulos 2001] of the coefficient of friction of an a-C film versus sliding distance for $P = 400\ \mu N$.

Film #	Thickness[a] (nm)	Roughness[a], rms (nm)	Normal load[a] (μN)	Coeff. of friction (peridynamics)	Coeff. of friction (experimental)[a]
1	31	0.51	50	0.132	0.16
			100	0.127	0.14
			200	0.115	0.13
			400	0.108	0.12
2	34	0.20	50	0.149	0.17
			100	0.128	0.15
			200	0.110	0.14
			400	0.099	0.12
3	39	0.15	50	0.156	0.18
			100	0.142	0.16
			200	0.121	0.14
			400	0.115	0.13
4	53	0.27	50	0.145	0.17
			100	0.127	0.15
			200	0.118	0.13
			400	0.102	0.12
5	59	0.23	50	0.140	0.17
			100	0.122	0.15
			200	0.114	0.14
			400	0.105	0.12
6	69	0.15	50	0.169	0.18
			100	0.148	0.16
			200	0.129	0.14
			400	0.121	0.13
7	95	0.24	50	0.147	0.17
			100	0.108	0.15
			200	0.115	0.13
			400	0.108	0.12

Table 5. Peridynamics and experimental results of the coefficient of friction of a-C films versus film thickness, roughness, and normal load. [a]Ref. [Lu and Komvopoulos 2001].

Figure 3 shows a comparison between peridynamics and experimental results of a typical coefficient of friction response for a 400 μN normal load. The peridynamics solution closely follows the experimental trend, showing good agreement with the average response of the scattered experimental data. Figure 3 and Table 5 illustrate the validity of the peridynamics friction model and provide justification for the modeling assumptions.

Figure 4 shows peridynamics results of the steady-state coefficient of friction (obtained as the average of all numerical data in the 0–4 μm sliding distance range) versus normal load for different a-C films
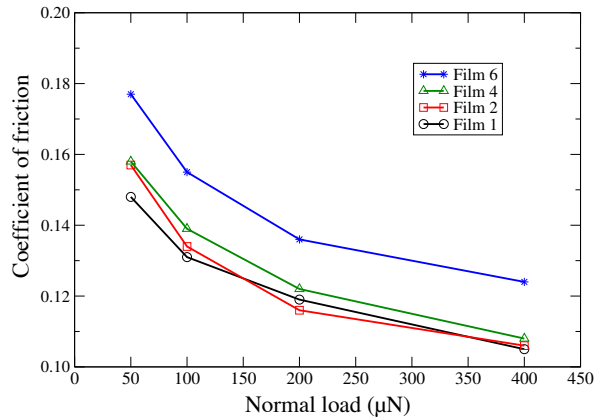
Figure 4. Peridynamics results of the coefficient of friction of various *a*-C films versus normal load.
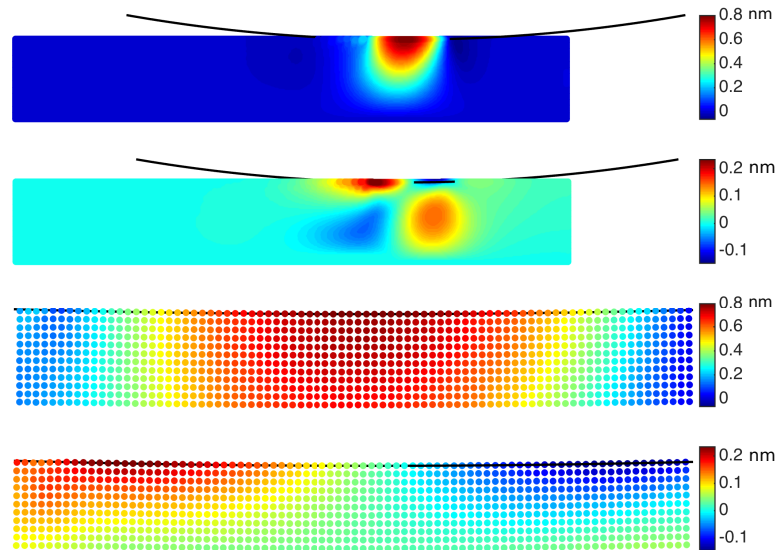

Figure 5. Contour maps of *y*-displacement (top image) and *x*-displacement (second image) of particles in film #4 for $x/S = 1$, and corresponding high-magnification contour maps (bottom two images) showing the displacement of particles in the near-surface region of the film adjacent to the contact interface with the sliding rigid tip.

(Table 2). All peridynamics solutions show that the coefficient of friction decreases with increasing normal load. This trend is in good agreement with experimental findings and is attributed to the inverse proportionality of the coefficient of friction of predominantly elastically deformed surfaces to the cubic root of the normal load [Lu and Komvopoulos 2001].

The top two images in Figure 5 show *y*- and *x*-displacement contour maps, respectively, for $x/S = 1$. High-magnification views of the particle displacements under the tip, shown in the bottom two images in Figure 5, provide insight into the highly stressed region of the film underneath the loaded tip. However,
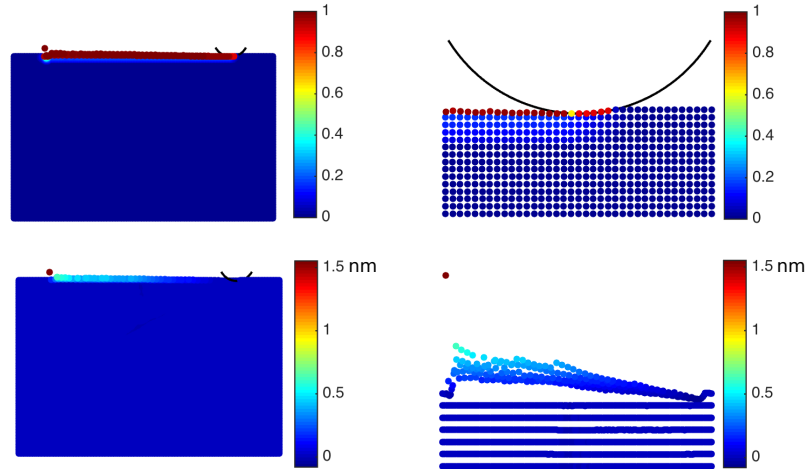
Figure 6. Top left: damage contour map of film #9 after tip unloading (damage index $D = 1$ corresponds to particles with all their bonds broken). Top right: corresponding high-magnification damage contour map of damaged particle layers in the near-surface region of the film. Bottom left: y-displacement contour map of damaged film #9 after tip unloading. Bottom right: corresponding high-magnification contour map showing the y-displacement of particles adjacent to the contact interface with the plowing rigid tip.

the zero displacements in the wake of the tip (top two images in Figure 5) reveal a full recovery of the unloaded film region. Importantly, despite the fully elastic behavior of the film/substrate medium and the adhesionless tip/film contact interface, the instantaneous coefficient of friction is not zero. Not only is this finding in contrast with classical friction theories, which attribute friction to irreversible deformation, but also reveals that frictionless contact is practically impossible.

5.2. *Wear depth.* To validate the peridynamics wear model, the experimentally measured depths of wear tracks produced on a-C film surfaces by a sharp conospherical rigid tip [Lu and Komvopoulos 2001] are compared with numerical results. Figure 6 (top left) shows damage at the film surface due to sliding contact interaction. A damage index $D = 1$ is indicative of bond breakage. As the rigid tip plows through the film, the particles near the surface are permanently displaced from their original positions. Figure 6 (top right) shows a close-up view of the deformed grid below the tip, revealing much more pronounced damage in the near-surface region of the a-C film adjacent to the sharp tip. Further insight into nanoscale film wear is provided by the y-displacement contour map and the close-up view of the near-surface damaged particle layers shown in Figure 6 (bottom left and right, respectively).

The wear depth is defined as the average displacement of all particles with partly broken bonds (i.e., $0 < D < 1$), located relatively far from the initial ($x/S = 0$) and final ($x/S = 1$) tip positions. The displacements of particles with $D = 1$ were not included in the calculation of the wear depth. Table 6 shows numerical and experimental results of the wear depth of three a-C films for $P = 10 \, \mu\text{N}$. For films #8 and #9 the agreement is very good ($\sim 4\%$ error), whereas for film #10 the agreement is fair, presumably because of the rougher film surface and errors due to the small film thickness (10 nm) relative to the grid size ($\approx 1.6 \, \text{nm}$).

Film #	Thickness (nm)	Roughness,[a] rms (nm)	Normal load (μN)	Wear depth (nm) (peridynamics)	Wear depth (nm) (experimental)[a]
8	17	0.19	10	0.730	0.76
9	22	0.18	10	0.391	0.40
10	10	0.20	10	0.161	0.20

Table 6. Comparison of peridynamics and experimental results of the wear depth of a-C films versus film thickness, roughness, and normal load. [a]Ref. [Lu and Komvopoulos 2001].

6. Conclusions

Nanoscale material behavior can be challenging because classical continuum theory breaks down at the nanoscale, whereas MD analysis is limited to very small scales of limited practical use. Peridynamics promises to bridge the material gap in computational mechanics. In this study, state-based peridynamics theory was used to develop friction and wear models of thin films. Favorable comparisons between peridynamics solutions and experimental results of thin films obtained under identical testing conditions illustrate the validity of the peridynamics friction and wear models developed in this study. Long-range forces were not considered and film surfaces were modeled as perfectly smooth, because the film roughness was significantly less than the grid size. Despite these assumptions, very good agreement was obtained between peridynamics and experimental results of films with thickness equal to or larger than 10 nm. The results of this study demonstrate the potential of peridynamics to capture the nanoscale tribological behavior of thin films, which is difficult (if not impossible) to achieve at the nanoscale with other numerical techniques, such as finite element analysis and the boundary element method.

Acknowledgments

References

[Agwai et al. 2008] A. Agwai, I. Guven, and E. Madenci, "Peridynamic theory for failure prediction in multilayer thin-film structures of electronic packages", pp. 1614–1619 in *58th Electronic Components and Technology Conference, IEEE* (Lake Buena Vista, FL, 2008), IEEE Service Center, Piscataway, NJ, 2008.

[Agwai et al. 2009] A. Agwai, I. Guven, and E. Madenci, "Damage prediction for electronic package drop test using finite element method and peridynamic theory", pp. 565–569 in *59th Electronic Components and Technology Conference, IEEE* (San Diego, CA, 2009), IEEE Service Center, Piscataway, NJ, 2009.

[Agwai et al. 2011] A. Agwai, I. Guven, and E. Madenci, "Crack propagation in multilayer thin-film structures of electronic packages using the peridynamic theory", *Microelectron. Reliab.* **51**:12 (2011), 2298–2305.

[Alali and Lipton 2012] B. Alali and R. Lipton, "Multiscale dynamics of heterogeneous media in the peridynamic formulation", *J. Elasticity* **106**:1 (2012), 71–103.

[Alder and Wainwright 1959] B. J. Alder and T. E. Wainwright, "Studies in molecular dynamics. I: General method", *J. Chem. Phys.* **31**:2 (1959), 459–466.

[Askari et al. 2006] E. Askari, J. Xu, and S. Silling, "Peridynamic analysis of damage and failure in composites", paper no. 2006–88 in *44th AIAA Aerospace Sciences Meeting and Exhibit* (Reno, NV, 2006), American Institute of Aeronautics and Astronautics, Reston, VA, 2006.

[Askari et al. 2008] E. Askari, F. Bobaru, R. B. Lehoucq, M. L. Parks, S. A. Silling, and O. Weckner, "Peridynamics for multiscale materials modeling", *J. Phys.: Conf. Ser.* **125**:1 (2008), 012078.

[Bobaru 2007] F. Bobaru, "Influence of van der Waals forces on increasing the strength and toughness in dynamic fracture of nanofibre networks: A peridynamic approach", *Model. Simul. Mater. Sci. Eng.* **15**:5 (2007), 397–417.

[Bobaru and Hu 2012] F. Bobaru and W. Hu, "The meaning, selection, and use of the peridynamic horizon and its relation to crack branching in brittle materials", *Int. J. Fract.* **176**:2 (2012), 215–222.

[Bobaru and Silling 2004] F. Bobaru and S. A. Silling, "Peridynamic 3D models of nanofiber networks and carbon nanotube-reinforced composites", pp. 1565–1570 in *Materials processing and design: Modeling, simulation and applications* (Columbus, OH, 2004), AIP Conf. Proc. **712**, 2004.

[Bobaru et al. 2009] F. Bobaru, M. Yang, L. F. Alves, S. A. Silling, E. Askari, and J. Xu, "Convergence, adaptive refinement, and scaling in 1D peridynamics", *Int. J. Numer. Methods Eng.* **77**:6 (2009), 852–877.

[Bobaru et al. 2011] F. Bobaru, S. A. Silling, and H. Jiang, "Peridynamic fracture and damage modeling of membranes and nanofiber networks", pp. 976–981 in *Proceedings of the 11th International Conference on Fracture, II* (Turin, Italy, 2005), Curran Associates, New York, 2011.

[Casiraghi et al. 2007] C. Casiraghi, J. Robertson, and A. C. Ferrari, "Diamond-like carbon for data and beer storage", *Mater. Today* **10**:1 (2007), 44–53.

[Celik et al. 2009] E. Celik, E. Oterkus, I. Guven, and E. Madenci, "Mechanical characterization of ultra-thin films by combining AFM nanoindentation tests and peridynamic simulations", pp. 262–268 in *59th Electronic Components and Technology Conference, IEEE* (San Diego, CA, 2009), IEEE Service Center, Piscataway, NJ, 2009.

[Charitidis 2010] C. A. Charitidis, "Nanomechanical and nanotribological properties of carbon-based thin films: A review", *Int. J. Refract. Met. Hard Mater.* **28**:1 (2010), 51–70.

[Grill 1999] A. Grill, "Diamond-like carbon: State of the art", *Diam. Relat. Mater.* **8**:2 (1999), 428–434.

[Ha and Bobaru 2010] Y. D. Ha and F. Bobaru, "Studies of dynamic crack propagation and crack branching with peridynamics", *Int. J. Fract.* **162**:1-2 (2010), 229–244.

[Ha and Bobaru 2011] Y. D. Ha and F. Bobaru, "Characteristics of dynamic brittle fracture captured with peridynamics", *Eng. Fract. Mech.* **78**:6 (2011), 1156–1168.

[Hu et al. 2011] W. Hu, Y. D. Ha, and F. Bobaru, "Modeling dynamic fracture and damage in a fiber-reinforced composite lamina with peridynamics", *J. Multiscale Comput. Eng.* **9**:6 (2011), 707–726.

[Hu et al. 2012] W. Hu, Y. D. Ha, and F. Bobaru, "Peridynamic model for dynamic fracture in unidirectional fiber-reinforced composites", *Comput. Methods Appl. Mech. Eng.* **217/220** (2012), 247–261.

[Kilic and Madenci 2010] B. Kilic and E. Madenci, "An adaptive dynamic relaxation method for quasi-static simulations using the peridynamic theory", *Theor. Appl. Fract. Mech.* **53**:3 (2010), 194–204.

[Kilic et al. 2009] B. Kilic, A. Agwai, and E. Madenci, "Peridynamic theory for progressive damage prediction in center-cracked composite laminates", *Compos. Struct.* **90**:2 (2009), 141–151.

[Komvopoulos et al. 1985] K. Komvopoulos, N. Saka, and N. P. Suh, "The mechanism of friction in boundary lubrication", *J. Tribol.* (*ASME*) **107**:4 (1985), 452–462.

[Lehoucq and Silling 2008] R. B. Lehoucq and S. A. Silling, "Force flux and the peridynamic stress tensor", *J. Mech. Phys. Solids* **56**:4 (2008), 1566–1577.

[Lifshitz 1996] Y. Lifshitz, "Hydrogen-free amorphous carbon films: Correlation between growth conditions and properties", *Diam. Relat. Mater.* **5**:3 (1996), 388–400.

[Lipton 2014] R. Lipton, "Dynamic brittle fracture as a small horizon limit of peridynamics", *J. Elasticity* **117**:1 (2014), 21–50.

[Liu and Hong 2012] W. Liu and J.-W. Hong, "Discretized peridynamics for brittle and ductile solids", *Int. J. Numer. Methods Eng.* **89**:8 (2012), 1028–1046.

[Lu and Komvopoulos 2001] W. Lu and K. Komvopoulos, "Nanotribological and nanomechanical properties of ultrathin amorphous carbon films synthesized by radio frequency sputtering", *J. Tribol.* (*ASME*) **123**:3 (2001), 641–650.

[Luan and Robbins 2005] B. Luan and M. O. Robbins, "The breakdown of continuum models for mechanical contacts", *Nature* **435**:7044 (2005), 929–932.

[Marshall and Evans 1984] D. B. Marshall and A. G. Evans, "Measurement of adherence of residually stressed thin films by indentation. I: Mechanics of interface delamination", *J. Appl. Phys.* **56**:10 (1984), 2632–2638.

[Parks et al. 2008] M. L. Parks, R. B. Lehoucq, S. J. Plimpton, and S. A. Silling, "Implementing peridynamics within a molecular dynamics code", *Comput. Phys. Commun.* **179**:11 (2008), 777–783.

[Parks et al. 2010] M. L. Parks, P. Seleson, S. J. Plimpton, S. A. Silling, and R. B. Lehoucq, "Peridynamics with LAMMPS: A user guide v0.3 beta", Report 2011-8523, Sandia National Labs, 2010, http://prod.sandia.gov/techlib/access-control.cgi/2011/118523.pdf.

[Silling 2000] S. A. Silling, "Reformulation of elasticity theory for discontinuities and long-range forces", *J. Mech. Phys. Solids* **48**:1 (2000), 175–209.

[Silling and Askari 2005] S. A. Silling and E. Askari, "A meshfree method based on the peridynamic model of solid mechanics", *Comput. Struct.* **83**:17 (2005), 1526–1535.

[Silling and Bobaru 2005] S. A. Silling and F. Bobaru, "Peridynamic modeling of membranes and fibers", *Int. J. Non-Linear Mech.* **40**:2-3 (2005), 395–409.

[Silling and Lehoucq 2008] S. A. Silling and R. B. Lehoucq, "Convergence of peridynamics to classical elasticity theory", *J. Elasticity* **93**:1 (2008), 13–37.

[Silling et al. 2007] S. A. Silling, M. Epton, O. Weckner, J. Xu, and E. Askari, "Peridynamic states and constitutive modeling", *J. Elasticity* **88**:2 (2007), 151–184.

[Volinsky et al. 2002] A. A. Volinsky, N. R. Moody, and W. W. Gerberich, "Interfacial toughness measurements for thin films on substrates", *Acta Mater.* **50**:3 (2002), 441–466.

[Xu et al. 2008] J. Xu, A. Askari, O. Weckner, and S. Silling, "Peridynamic analysis of impact damage in composite laminates", *J. Aerosp. Eng.* (*ASCE*) **21**:3 (2008), 187–194.

SAYNA EBRAHIMI: sayna@berkeley.edu
Department of Mechanical Engineering, University of California, Berkeley, CA 94720-1740, United States

DAVID J. STEIGMANN: dsteigmann@berkeley.edu
Department of Mechanical Engineering, University of California, Berkeley, 6133 Etcheverry Hall, Berkeley, CA 94720-1740, United States

KYRIAKOS KOMVOPOULOS: kyriakos@me.berkeley.edu
Department of Mechanical Engineering, University of California, Berkeley, 5143 Etcheverry Hall, Berkeley, CA 94720-1740, United States

JOURNAL OF MECHANICS OF MATERIALS AND STRUCTURES

msp.org/jomms

Founded by Charles R. Steele and Marie-Louise Steele

Cover photo: Wikimedia Commons

Special issue on
Peridynamic Theory